

# OCT elastography: imaging microscopic deformation and strain of tissue

Joseph M. Schmitt

*Department of Electrical and Electronic Engineering  
Hong Kong University of Science and Technology*

*eeschmit@ee.ust.hk*

**Abstract:** Optical coherence tomography (OCT) has been applied to the study of the microscopic deformation of biological tissue under compressive stress. We describe the hardware and theory of operation of an OCT elastography system that measures internal displacements as small as a few micrometers by using 2D cross-correlation speckle tracking. Results obtained from gelatin scattering models, pork meat, and intact skin suggest possible medical applications of the technique.

©1998 Optical Society of America

**OCIS codes:** (170.4500) Optical coherence tomography; (120.6160) Speckle interferometry; (120.4290) Nondestructive testing

---

## References

1. K. J. Parker, L. Gao, R. M. Lerner, and S. F. Levinson, "Techniques for elastic imaging: A review," *IEEE Eng. Med. Biol. Mag* **15**, 52-59 (1996).
2. J. Ophir, I. Céspedes, H. Ponnekanti, Y. Yazdi, and X. Li, "Elastography: a quantitative method for imaging the elasticity of biological tissues," *Ultras. Imaging* **13**, 111-134 (1991).
3. A. P. Sarvazyan, A. R. Skovoroda, S. Y. Emelianov, J. B. Fowlkes, J. G. Pipe, R. S. Adler, R. B. Buxton, and P. L. Carson, "Biophysical bases of elasticity imaging," *Acoust. Imaging* **21**, 223-240 (1995).
4. Y. Yamakoshi, J. Sato, and T. Sato, "Ultrasonic imaging of internal vibration of soft tissue under forced vibration," *IEEE Trans. Ultras., Ferro., Freq. Control* **37**, 223-240 (1990).
5. D. Huang, E. A. Swanson, C. P. Lin, J. S. Schuman, W. G. Stinson, W. Chang, M. R. Hee, T. Flotte, K. Gregory, C. A. Puliafito, and J. G. Fujimoto, "Optical coherence tomography," *Science* **254**, 1178-1181 (1991).
6. A. F. Fercher, C. K. Hitzenberger, W. Drexler, G. Kamp, and H. Sattmann, "In vivo optical coherence tomography," *Am. J. Ophthalmol.* **116**, 113-114 (1993).
7. J. A. Izatt, M. Kulkarni, K. Kobayashi, M. V. Sivak, J. K. Barton, and A. J. Welsh, "Optical coherence tomography for biondiagnostics," *Optics and Photonics News* **8**, 41-47 (1997).
8. B. Bouma, G. J. Tearney, S. A. Boppart, M. R. Hee, M. E. Brezinski, and J. G. Fujimoto, "High resolution optical coherence tomographic imaging using a mode-locked Ti:Al<sub>2</sub>O<sub>3</sub> laser source," *Opt. Lett.* **20**, 1486-1488 (1995).
9. J. A. Smith, R. Muthupillai, P. J. Rossman, T. C. Hulshizer, J. F. Greenleaf, and R. L. Ehman, "Characterization of biomaterials using magnetic resonance elastography," *Rev. Progr. Quantitat. NonDestr. Eval.* **2**, 1323-1330 (1997).
10. J. M. Schmitt and A. Knüttel, "Model of optical coherence tomography of heterogenous tissue," *J. Opt. Soc. Am. A* **14**, 1231-1242 (1997).
11. T. Varghese, M. Bilgen, and J. Ophir "Multiresolution imaging in elastography," *IEEE Trans. Ultras., Ferro., Freq. Control* **45**, 65-75 (1998).
12. J. M. Schmitt, S. L. Lee, and K. M. Yung, "An optical coherence microscope with enhanced resolving power," *Opt. Commun.* **142**, 203-207 (1997).
13. R. E. Boucher and J. C. Hassab, "Analysis of discrete implementation of generalized cross correlator," *IEEE Trans. Acoust. Speech, Signal Proc.* **29**, 609-611 (1981).

---

## 1. Introduction

Many diseases of soft tissue progress to a stage in which changes in the mechanical properties of the tissue can be discerned. For example, when an atherosclerotic lesion in the wall of a blood vessel calcifies, it becomes noticeably stiffer than the surrounding

tissue. Similarly, breast and testicular cancers often reveal themselves to the sufferer as lumps or nodules distinguished by their unusual hardness. Pathological processes may also reduce rather than increase tissue hardness, as in certain infectious diseases that break down the extracellular tissue matrix.

Ultrasonic elastography, a technique that has been under development for about 10 years,[1,2] aims to exploit local changes in the elastic or shear modulus of a tissue as a contrast mechanism for improving the detectability of lesions in B-mode ultrasound images. The basic idea is to image the displacements of individual tissue elements as they are stretched, compressed, or vibrated. From the resultant deformation pattern, the local strain is estimated assuming that the applied stress is uniform or has a known distribution. To quantify the displacements, one- or two-dimensional speckle tracking methods based on cross-correlation analysis are employed. Knowledge of the internal displacement field permits estimation of the local strain for a known applied stress. Like water, soft tissue is nearly incompressible and conserves its volume under pressure. Therefore, provided that the stress applied is small enough such that the non-linearity of the elastic constants can be neglected, only the shear modulus  $G$  (or, equivalently, the Young's modulus  $E$ , given by  $E = 3G$  for an incompressible material), is needed to characterize the elastic properties of tissue in a given direction under static conditions.[3] The main challenge of static-mode elastography, in which a constant stress is applied to the surface of a tissue, is to image the spatial distribution of  $G$ . By applying a time-varying stress, the viscoelastic properties of tissue can also be characterized.[4] Neither of these modes of ultrasonic elastography, however, has yet been proven to improve the detectability of lesions in clinical practice.

In this study we set out to explore elastography on a scale substantially smaller than that investigated previously by using ultrasonic methods. We applied optical coherence tomography (OCT) to image micrometer-level displacement and strain distributions induced by compression of soft tissues. OCT is an interferometric imaging method that takes advantage of the short coherence lengths of broadband light sources to achieve precise axial sectioning in highly scattering media.[5,6,7] Earlier studies have substantiated the ability of OCT to resolve structures with dimensions as small as a few micrometers at depths up to 1- 2 mm below the surface of optically dense tissues.[8] The experiments reported in this paper demonstrate that OCT can quantify internal displacements as small as a few micrometers in experimental scattering models, pork meat, and living skin. The minimum resolvable displacement is at least an order of magnitude below that measured with the highest frequency ultrasonic transducers (10 MHz) used routinely in clinical practice [1] and exceeds the minimum displacement that has been measured by magnetic resonance imaging (MRI) by an even larger magnitude. [9] Thus, a primary strength of OCT-based elastography is its potential to evaluate the mechanics of intact tissue on a scale that has been out of the reach of clinical investigators. The price paid for this high resolving power is the shallow depth over which the measurements can be obtained (typically 0 - 1 mm), a limitation from which ultrasonic- and MRI-based elastography do not suffer.

## 2. Theory of OCT elastography

Like its ultrasonic counterpart, OCT elastography relies on speckle tracking to estimate relative motion of subsurface structures imaged under different applied stresses. Interference images acquired by OCT systems can be modeled approximately in the form of a convolution,

$$I(r, z) = \exp(-2\bar{\mu}_s z) \int_{-\infty}^{\infty} \int_{-\infty}^{\infty} \sigma_b(r, z) h(r - r', \tau - \tau') r' dr' d\tau'$$

$$= \exp(-2\bar{\mu}_s z) [\sigma_b(r, z) * h(r, \tau)] \quad (1)$$

where  $r$  and  $z$  denote the radial and depth coordinates measured along axes perpendicular to and parallel to the axis of the focused sample beam, respectively,  $\sigma_b(r, z)$  is a function that represents the sample as a distribution of points with different backscattering cross sections, and  $h(r, \tau)$  is the point-spread function of the OCT system. The quantity outside the integral approximates the attenuation of the beam as an exponential function of the mean of the scattering coefficient,  $\bar{\mu}_s$ , averaged over the illuminated volume. The PSF of OCT systems that employ light-emitting diode sources are approximated well by a separable function proportional to the product of the temporal autocorrelation function of the source  $\Gamma(\tau)$  and the radial pupil function  $p(r)$  of the source-detection optics,[10]

$$h(r, \tau) = \Gamma(\tau)p(r) \quad (2)$$

By assuming that the source has a Gaussian-shaped frequency spectrum, we can write the temporal autocorrelation function explicitly as

$$\begin{aligned} \Gamma(\tau) &= \text{Re}[\langle \mathbf{E}_s(t) \mathbf{E}_s^*(t + \tau) \rangle] \\ &= \exp(-\tau^2 / \tau_c^2) \cos(2k_0 c \tau) \end{aligned} \quad (3)$$

where  $\mathbf{E}_s$  is the vector electric field amplitude of the source and  $k_0 = 2\pi/\lambda_c$  is the optical wavenumber corresponding to the central free-space wavelength  $\lambda_c$  of the source. The optical delay  $\tau$  represents the difference between the lengths of the optical paths in the reference and sample arms of the interferometer with  $\tau_c$  equal to the source coherence time. If we assume that the paths are matched when the sample volume is centered on a point scatterer, then  $\tau = 2n\Delta z/c$ , where  $c$  is the speed of light in free space,  $n$  is the mean refractive index of the medium, and  $\Delta z$  is the axial distance of the center of the sample volume from the scatterer. For a source with a Gaussian-shaped frequency spectrum and a FWHM spectral bandwidth  $\Delta\lambda$ , the coherence time is  $\tau_c = 2(\ln 2)\lambda^2/(\pi c \Delta\lambda)$ . In the diffraction limit, the focal length,  $f$ , of the objective lens and the sample beam's 1/e intensity diameter,  $D$ , determine the lateral extent of the pupil function:

$$p(r) = \exp \left[ -r^2 / \left( \frac{4f^2}{k_0^2 D^2} \right) \right] \quad (4)$$

Consider a single point scatterer embedded in the medium at the position  $(r, z)$  at which the optical pathlengths of the two arms of the interferometer are matched (i.e.,  $\tau = 0$ ). The primary effect of applying stress to the medium is to displace the scatterer from its original position to a new location  $(r + r_d, z + z_d)$ . From Eq.(1), we find

$$\begin{aligned} I_1(r, z) &= [\delta(r, z) \sigma_b * h(r, \tau)] \exp(-2\bar{\mu}_s z) \\ &= h(0, 0) \sigma_b \exp(-2\bar{\mu}_s z) \end{aligned} \quad (5)$$

for the pre-stressed interference image and

$$\begin{aligned} I_2(r, z) &= [\delta(r + r_d, z + z_d) \sigma_b * h(r, \tau)] \exp(-2\bar{\mu}_s z) \\ &= h(r_d, 2nz_d/c) \sigma_b \exp(-2\bar{\mu}_s z) \end{aligned} \quad (6)$$

after application of the stress. One technique for measuring the displacement vector  $(r_d, z_d)$  is to first compute the normalized cross correlation of the interference images of the pre-stressed and stressed medium within a pre-defined window,

$$\rho(r', z') = \frac{\int_{-Z/2}^{Z/2} \int_{-R/2}^{R/2} I_1(r, z) I_2(r - r', z - z') dr dz}{\sqrt{\int_{-Z/2}^{Z/2} \int_{-R/2}^{R/2} I_1^2(r, z) dr dz \int_{-Z/2}^{Z/2} \int_{-R/2}^{R/2} I_2^2(r - r', z - z') dr dz}} \quad (7)$$

and then estimate the displacement from the maximum of the resultant cross-correlation function,

$$\hat{r}_d = \max\{\rho(r', z')\} \quad \text{for } z' = 0, -R/2 \leq r' \leq R/2. \quad (8)$$

$$\hat{z}_d = \max\{\rho(r', z')\} \quad \text{for } r' = 0, -Z/2 \leq z' \leq Z/2 \quad (9)$$

For our hypothetical isolated point scatterer, it can be seen by substituting Eqs. (5) and (6) into Eq. (7) that  $\rho$  is maximum for  $r' = r_d$  and  $z' = z_d$ , assuming that the displacement is small enough such that  $\bar{\mu}_s z_d \ll 1$ . In this case the radial and axial displacement estimates are exact; however, in the more realistic case in which numerous scatterers are present in the sample volume, the periodicity of the coherent point response  $h(r, \tau)$  makes the estimates  $\hat{r}_d$  and  $\hat{z}_d$  susceptible to interference noise. Moreover, when either the window over which the cross-correlation is calculated or the induced strain is large, the effect of the applied stress cannot be modeled strictly by translation of the scatterers; the distortion of the scatterer distribution, which reduces the maximum of  $\rho$ , must be taken into account.[11]

Our experience suggests that cross correlating the envelopes rather than the complex magnitudes of the interference signals backscattered from dense scattering tissues yields more stable estimates of  $r_d$  and  $z_d$ . For this approach to be effective, the envelope of  $h(r, \tau)$  should be made as narrow as possible by using a source with the widest possible bandwidth to maximize the signal-to-noise ratio for correlation estimates. Interference noise can be reduced further by using the widest possible numerical aperture of the detection optics in conjunction with angular compounding using multiple detectors. The OCT system described in the following section implements all of these measures.

As the results in Section 5 illustrate, viewing a sequence of OCT images of internal displacements of a tissue under gradually increasing compressive stresses can, in some cases, provide sufficient information to enable a knowledgeable observer to deduce regional variations in tissue stiffness without the need for further processing. However, when the tissue structure is complex or the induced strains are small, deducing the stiffness by viewing displacement images can be difficult. Quantitative elastic imaging requires estimation of the differential strain, defined as

$$\vec{s}(r, z) = \lim_{\Delta r, \Delta z \rightarrow 0} \frac{\vec{d}(r, z) - \vec{d}(r + \Delta r, z + \Delta z)}{\sqrt{(\Delta r)^2 + (\Delta z)^2}} \quad (10)$$

where  $\vec{d}(r, z)$  and  $\vec{d}(r + \Delta r, z + \Delta z)$  are the displacement vectors at neighboring points. The strain in the axial (depth) direction, an important quantity for evaluation of stiffness under compressive stress, is estimated from the displacements measured at two points on the  $z$  axis,

$$\hat{s}_z(r, z) \simeq \frac{\Delta d_z}{\Delta z} = \frac{\hat{d}_z(r, z) - \hat{d}_z(r, z + \Delta z)}{\Delta z} \quad (11)$$

When the applied stress is known, the regional variation of the elastic or shear modulus can be estimated from the strain distribution.

### 3. Experimental methods

#### 3.1 OCT elastography system

Fig. 1 shows the experimental setup with which the elastography experiments were carried out. At the heart of the system is an OCT scanner built around a free-space Michelson interferometer. The principles of operation of the scanner, which employs dual light-emitting diode (LED) sources, 4-channel angular compounding, and dynamic focusing

to improve its performance, are described in an earlier publication [12]. The FWHM widths of the axial and radial PSFs of the scanner measured in a single-scattering tissue model with a refractive index of 1.36 are approximately  $7\text{ }\mu\text{m}$  and  $5\text{ }\mu\text{m}$ , respectively. The outputs of two LEDs are combined to narrow the width of the axial PSF. Because the center wavelengths (1260 nm and 1300 nm) of the two LEDs differ by the sum of their half-bandwidths, the coherence length is approximately one-half of that of a single LED. The dynamic-focusing arrangement keeps the lateral PSF approximately constant throughout the range of probing depths.

The tissue compressor consists of a piezoelectric actuator (Physik Instrumente Model P-720) with a circular glass cover slip (1.8 cm diameter) glued to its ring-shaped head. Originally designed for auto-focusing applications, the actuator employs mechanical amplification by hinged flexure joints to achieve linear displacements of 0 - 100  $\mu\text{m}$  for input voltages in the range of 0 - 100 V. The glass cover slip serves a dual role as an optical window and a compression plate. The objective lens in the sample arm of the interferometer focuses the sample beam through the cover slip to points below the surface of the tissue. As the actuator expands, the cover slip applies uniform pressure to the tissue, compressing its surface inward along the axis of the sample beam.

We configured the compressor to operate in one of two modes: the frame mode and the line-by-line mode. In the frame mode, a constant voltage is applied to the actuator during acquisition of an entire cross-sectional image. The next image is acquired after the voltage has been increased by a small step (typically 10 volts or less) and the step-wise increase in compressive stress continues until an entire sequence of images has been completed. In the line-by-line mode, the voltage applied to the actuator is synchronized with the lateral scanning movement of the stage. Just before each axial depth scan ('A-line') is acquired, the tissue is compressed a pre-determined amount by applying a voltage to the actuator. After completion of the scan, the voltage is turned off to release the tissue and the stage moves laterally by a single step before acquiring the next A-line. Data is collected during the compression phase only rather than during both the compression and release phases to reduce the influence of the mechanical hysteresis of the tissue. This process of alternatively compressing and releasing the tissue repeats until the entire cross-sectional image has been scanned.

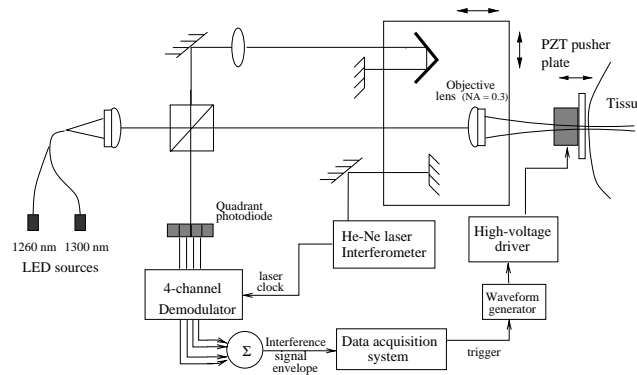


Figure 1. Setup of experimental elastography system built around a scanning white-light interferometer.

The frame mode of operation is suitable for elastography of samples that can be held still for a period long enough to acquire multiple images. A primary advantage of this mode of operation is that compressive deformation of internal structure can be tracked nearly continuously over a wide range. Although adequate for elastography

of the excised tissue and the tissue models, the image acquisition period of the OCT system used in this study was too long for accurate elastic imaging of skin *in vivo*. We observed that viscoelastic relaxation and creep, pulsatile blood flow, and respiration caused unacceptable errors in the displacement estimates over the 20-second period required to obtain a single  $256$  (lateral)  $\times$   $512$  (depth) pixel image. The line-by-line operation mode was found to be better suited for *in vivo* elastography because adjacent A-lines could be acquired in quick succession to reduce the displacement errors caused by undesired tissue motion. As configured for this study, the OCT system had an axial scan rate of  $11$  Hz, yielding an acquisition time of less than  $200$  ms for a pair of adjacent A-lines, which is about  $100$  times shorter than the frame acquisition time. In the line-by-line mode, acquisition of a single pair of A-lines is sufficient for measurement of axial displacement alone; measurement of both lateral and axial displacement can be accomplished by processing a group of neighboring A-lines. The principal drawback of this mode of operation is that tissue strain must be estimated from a single pulse of applied stress rather than from a series of gradually increasing stresses. Consequently, algorithms that take advantage of the continuity of the deformation to reduce noise cannot be applied. In addition, the acquisition speed is limited by the need to allow sufficient time for relaxation of the tissue between compression-release cycles.

### 3.2 Tissues and tissue models

Three types of samples were used to evaluate the feasibility and potential utility of OCT elastography in tissue imaging applications: gelatin tissue models, pork meat, and intact human skin.

The gelatin models consisted of a mixture of  $0.2\text{ }\mu\text{m}$ - and  $6\text{ }\mu\text{m}$ -diameter polystyrene latex spheres distributed in solid block of gelatin. The models were made with a high concentration of gelatin powder ( $10\%$  by weight) in water to approximate the stiffness of a tissue containing a similar concentration of fibrous protein. To simulate the multiple backscatter that appears as speckle in OCT images of dense tissue, we set the average volume fraction of small-diameter latex spheres in the model to  $0.5\%$ . This concentration was high enough to ensure that numerous ( $\approx 200$ ) spheres were present within the  $5\times 5\times 7\text{ }\mu\text{m}^3$  sample volume of the OCT system. For easy visualization of the larger spheres, their volume fraction was also set to  $0.5\%$ , which made the average separation between spheres greater than the source coherence length. The scattering coefficient of the gelatin model, computed by Mie theory using values of  $1.59$  and  $1.35$  for the refractive indices of polystyrene and the gelatin, respectively, was  $2.3\text{ mm}^{-1}$  at the central wavelength of the combined light sources ( $1280\text{ nm}$ ). The deformation measurements were performed on a square block of the gelatin model  $3\text{ mm}$  wide and  $2\text{ mm}$  thick into the base of which a small volume of cyanoacrylic glue was injected. After solidification, the glue formed a hard nondeformable mass that adhered to the protein in the surrounding gelatin.

Pork meat obtained from a local slaughterhouse was used to test the ability of the OCT elastography to probe the mechanical properties of a tissue of mixed composition under controlled laboratory conditions. A square block of the meat, approximately  $1\text{ cm}$  wide and  $0.3\text{ cm}$  thick, was dissected from a region containing streaks of fat interposed between layers of muscle fiber. Because the meat was refrigerated for an extended period (more than  $24$  hours) and the measurements were done at room temperature ( $20^\circ\text{C}$ ) instead of body temperature, it is likely that both the mechanical and optical properties of the muscle and adipose tissue differed significantly from those of corresponding tissues *in vivo*.

To test the feasibility of performing elastography *in vivo*, we imaged compressive deformation of the skin in the region above the most distal joint on the back side of

the index finger of an adult male subject. The surface of the bone, located about 2 mm below the surface of the skin and wrapped tightly in a stiff tendon sheath, provided an immobile base against which the skin was pressed.

### 3.3 Measurement procedures

The same procedure was followed to collect sequences of OCT images of the gelatin models and samples of pork meat for elastography. Each sample was inserted between a rigid metal plate and the glass window of the compressor, indented approximately 0.3 mm, and held in this position for at least a minute to permit residual strain in the sample to dissipate. Then, operating in the frame mode, the OCT system collected a sequence of cross-sectional images from each sample as it was compressed in steps of 5 or 10  $\mu\text{m}$ .

OCT images of living skin for elastography were obtained in the line-by-line mode. The palmar surface of the finger was clamped to the rigid plate by a custom-made holder. The free surface of the finger was pressed against the glass window of the compressor until the finger indented about 0.3 mm. The finger was held in this position for at least a minute to allow internal strain to dissipate. The peak-to-peak magnitude of the voltage applied to the piezoelectric actuator was set to produce a 20  $\mu\text{m}$  displacement of the finger's surface at the peak of each compression cycle, with 1  $\mu\text{m}$  lateral movement between cycles. The total lateral scan distance was 0.8 mm over a period of about 70 s.

We carried out a separate experiment to quantify the stress applied to the finger in the elastography experiments and to estimate the bulk elastic modulus of skin at different levels of compression. In this experiment an electronic pressure transducer was interposed between the compressor plate and the skin. As the displacement of the compression plate was varied continuously over a 0-50  $\mu\text{m}$  range by applying a 2 Hz triangular voltage waveform to compressor, the output voltage of the pressure transducer was recorded. For estimating the applied pressure from the measured force, the contact area on the skin was measured by tracing the boundaries of the finger on the glass plate. These measurements were repeated for different compressive preloads to characterize the dependence of the bulk elastic modulus on the applied stress.

## 4. Image processing methods

The flow chart in Fig. 2 summarizes the processing steps that were used to derive displacement and strain information from images of a pre-stressed and stressed tissue or gelatin model. To form a pair of images from data acquired in the line-by-line mode, the A-lines recorded during the compression phase and the release phase were grouped separately. The image data acquired in the frame mode were processed pair-by-pair and the total displacement at a given pixel was computed as the vector sum of the displacement estimates for each image pair. The pixel  $(i_0, j_0)$  with the maximum intensity in a  $4 \times 4$  block of pixels served as the centerpoint around which the cross-correlations were computed. To compute the cross correlation function, we used a discretized form of Eq. (7),

$$\rho(i, j) = \frac{\sum_{i=-M/2}^{M/2} \sum_{j=-N/2}^{N/2} I_1(i_0, j_0) I_2(i_0 - i, j_0 - j)}{\sqrt{\sum_{i=-M/2}^{M/2} \sum_{j=-N/2}^{N/2} I_1^2(r, z) \sum_{i=-M/2}^{M/2} \sum_{j=-N/2}^{N/2} I_2^2(i_0 - i, j_0 - j)}} \quad (12)$$

Quadratic interpolation [13] was then used to find the displacements  $\hat{r}_d$  and  $\hat{z}_d$  at which the cross-correlation was largest within a given block. The dimension of the  $M \times N$  block over which the cross-correlation calculation was performed was optimized by trial and error to obtain the best estimates, as judged by the ratio of the mean and standard

deviations of  $\hat{r}_d$  and  $\hat{z}_d$ . For the results reported in this paper, the optimum block sizes ranged from  $7 \times 7$  to  $16 \times 16$  pixels<sup>2</sup> for interpixel distances equal to  $2 \mu\text{m}$  in both dimensions. Eq. (11) was used to compute axial strain, with the separation distance  $\Delta z$  set equal to the center-to-center distance between blocks. Displacements were not computed in regions of the images in which the magnitudes of the interference signals fell below twice the level of the electronic noise; pixels in these regions were excluded from the analysis.

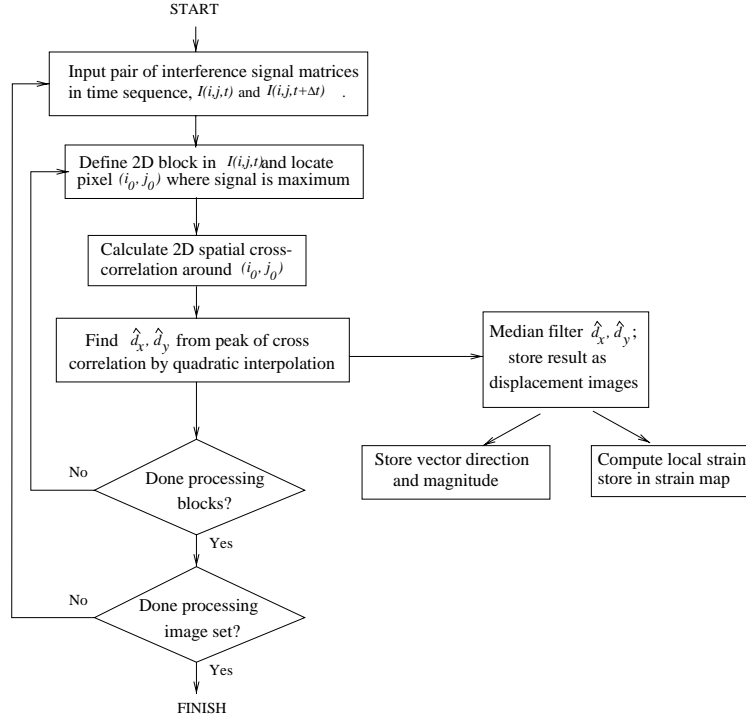


Figure 2. Image processing steps used to obtain quantitative estimates of local displacement and strain.

## 5. Results and Discussion

The 10-frame movie in Fig. 3 shows a series of OCT images recorded during step-wise compressive deformation of a gelatin model. Appearing as bright white spots in the images, the  $6 \mu\text{m}$  spheres move along nearly continuous trajectories that can be traced visually. The  $0.2 \mu\text{m}$  spheres, which are not resolvable, generate a fine speckle pattern that changes rapidly as the compression proceeds. Careful examination of the image sequence shows non-uniform displacement of the  $6 \mu\text{m}$  spheres which suggests the presence of a stiff mass in the lower center of the gel. The mass (hardened glue), whose location is outlined in Fig. 4, backscatters poorly and appears as an extended region of low reflectivity in the OCT images. The portion of the gel in the upper right corner appears to move axially and to cause the gel below it to bulge slightly to the right. The pattern of the deformation is displayed in Fig. 5 as an array of vectors that indicate the magnitudes and direction of the calculated axial and lateral displacements at different locations. This vector diagram quantifies the particle trajectories that can be followed roughly by eye in the movie sequence.



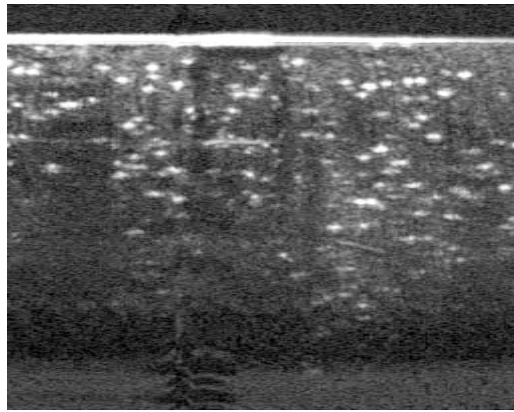


Figure 3. 10-frame movie showing a sequence of OCT images taken during step-wise compression of a gelatin phantom ( $5\ \mu\text{m}$  displacement of the top surface per step). The dimensions of the images are  $1\ \text{mm}$  (width)  $\times$   $1\ \text{mm}$  (depth) and the intensities are mapped onto a logarithmic gray scale.

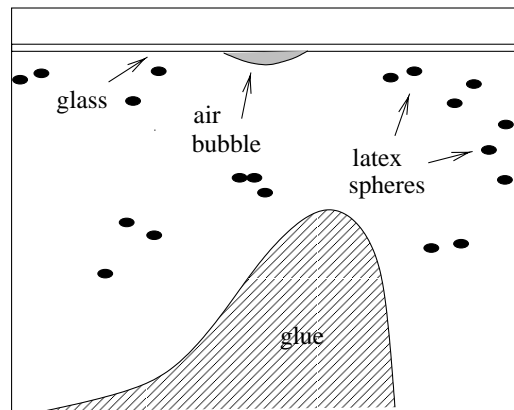


Figure 4. Internal structure of the gelatin scattering model from which the sequence of images in Fig. 3 were obtained.

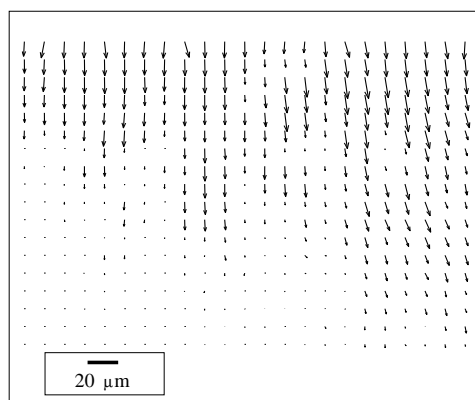


Figure 5. Displacement vector field  $\vec{d}(r, z)$  measured for the gelatin model sequence over the first 5 frames. The bar gives the scale of the vector lengths.

The previous example illustrates that the deformation pattern seen in a sequence of OCT images of a scattering material recorded under increasing compressive stress can reveal the presence of an object whose elasticity differs substantially from that of its surroundings. How well does this approach work in a biological tissue that is composed of structures with more subtle variations in their mechanical properties? Unfortunately, because of the problem of tissue motion discussed in Section 3.1, our present OCT system is not fast enough to record a sequence of images from living tissue under compression. As an alternative, we recorded image sequences *in vitro* from samples of pork meat. The 5-frame movie in Fig. 6 shows one such sequence. The displacements of the internal structures in this sample appear more uniform than those of the gelatin model, but spatial variations can still be discerned. In the area of the image labeled 'fat' in Fig. 7, the tissue close to the surface moves noticeably more than the tissue below it, indicative of the behavior of a spring under compression. In contrast, the region labeled 'muscle' behaves more like a rigid body that translates without discernible compression. These differences reflect the disparity in the stiffness of these tissues. Fig. 8a shows an image of the axial displacements that was created by using the image processing techniques outlined in Section 4.

The differential strains measured by fitting the slope of the axial displacements  $\hat{d}_z$  over image blocks of the same size ( $50\text{ }\mu\text{m}$  wide and  $100\text{ }\mu\text{m}$  deep) in the regions marked '1' and '2' in Fig. 8a are plotted in Fig. 8b. The mean axial displacements in these regions were approximately  $10\text{ }\mu\text{m}$  and  $16\text{ }\mu\text{m}$ , respectively. Consistent with the higher elasticity of fat than muscle, the strain measured for Region 2 was about 15 times greater than the strain measured in Region 1 (6.0% versus 0.41%). According to estimates reported by Sarvazyan *et al.*, [3] the ratio of the elastic moduli of muscle and fat *in vivo* may be as high as  $10^2 - 10^3$ . We attribute the relatively lower ratio measured in this study to the tendency of the fat to partially congeal at the temperature at which the measurements were made. To the extent that the elastic properties of the tissues in both regions were homogeneous, the root-mean square (rms) deviation of  $\hat{d}_z$  around each fitted line provides a good estimate of the minimum resolvable displacement that could be measured with the current OCT elastography setup under different conditions. In region 1, the rms deviation was  $0.2\text{ }\mu\text{m}$  and in Region 2, where the interference signals were weaker, the rms deviation was  $0.6\text{ }\mu\text{m}$ .

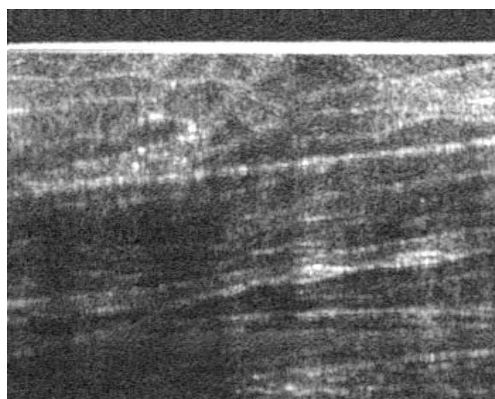


Figure 6. 5-frame movie showing a sequence of OCT images taken during stepwise compression of pork meat ( $10\text{ }\mu\text{m}$  displacement of the top surface per step). The dimensions of the images are  $1.2\text{ mm}$  (width)  $\times$   $0.7\text{ mm}$  (depth) and the intensities are mapped onto a logarithmic gray scale.

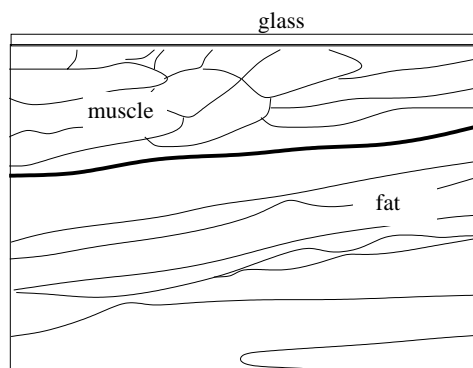


Figure 7. Internal composition of the pork meat sample, showing the location of the muscle and fat layers.

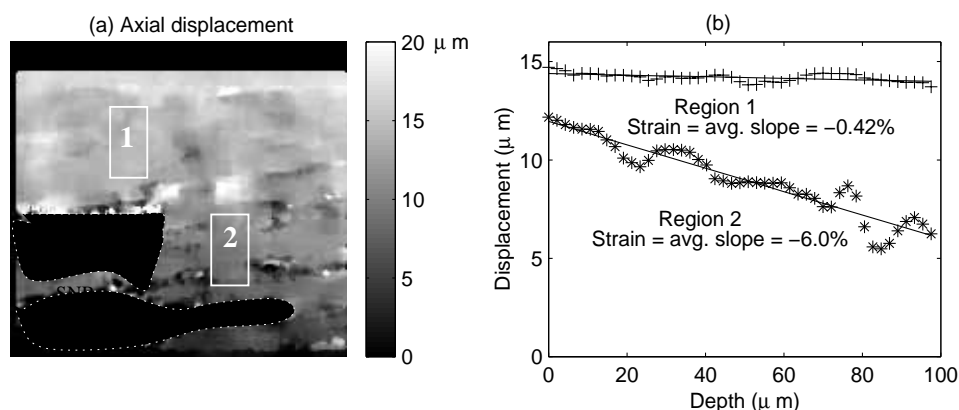


Figure 8. (a) Image of the axial displacements inside the pork meat sample, calculated by cross correlation analysis over the 5-frame sequence. The black areas outlined with dotted lines indicate where the signal-to-noise ratio was too low for calculation of the displacements, (b) Strains estimation for the areas marked '1' and '2' in the displacement image on the left.

The results of the *in vivo* experiments verify the ability of the OCT system to measure subsurface deformation of skin under compression. Figs. 9a and b show unprocessed and reconstructed images of skin acquired by the OCT elastography system operating in the line-by-line mode. The reconstructed image was formed by first calculating the displacements resulting from the applied stress using the cross-correlation method and then realigning the pixels. Comparison of the enlarged versions of the image before and after reconstruction (Figs. 9c and d) shows the effectiveness of the cross-correlation method. The axial and lateral displacement images of the skin are displayed in Fig. 10. Like that of the meat phantom, the displacement image of this region of the skin appears quite uniform, but spatial variations are still discernible. In particular, a small lateral shift ( $2\text{--}3\text{ }\mu\text{m}$ ) of the lower dermis half under compression is apparent (compare the lower left and upper right areas of Fig. 10). A shift of similar magnitude, which could occur in either direction, was seen in images taken from other regions of the skin. In contrast, the epidermis showed no measurable lateral shift or axial compression. We attribute this behavior to the unique layered structure of the skin: the relatively stiffer epidermis tends to transmit stress to the dermis below where the stress dissipates by displacing the tissue along the axis of connective fibers that run parallel

to the skin's surface. The distribution of axial displacements shown in Fig. 10b appears to have a barely distinguishable layered structure on which small regional variations are superimposed that do not correspond closely with the backscatter variations in the OCT images. Measured over the entire image, the mean axial displacement was  $13.7\ \mu\text{m}$ , with a standard deviation of  $0.45\ \mu\text{m}$ ; the mean lateral displacement was  $2.2\ \mu\text{m}$ , with a standard deviation of  $0.44\ \mu\text{m}$ . These standard deviations are close to those measured the pork meat in the frame mode, which suggests that comparable accuracy can be achieved in spite of tissue motion by using the line-by-line mode. What fraction of the observed variations corresponds to local variations in the elastic modulus of the tissue is still not clear. Further studies are needed to understand their origin.

Measured by using the procedure described in Section 3.3, the stress applied to the skin during the experiments ranged from about 1 to 3 g-force/ $\text{mm}^2$  for pre-load indentations of the skin's surface between 0.1 and 0.4 mm. The corresponding bulk shear modulus  $G$  measured with the OCT elastography system within this range increased from about  $6 \times 10^4\ \text{N/m}^2$  for the smallest indentation to  $1.3 \times 10^5\ \text{N/m}^2$  for the largest indentation. These magnitudes are in the range of those measured previously for the dermis by conventional methods.[3] Since the shear modulus of the epidermis is typically several orders of magnitude higher, these measurements suggest that strain induced in the bulk skin concentrates mostly in the dermis.

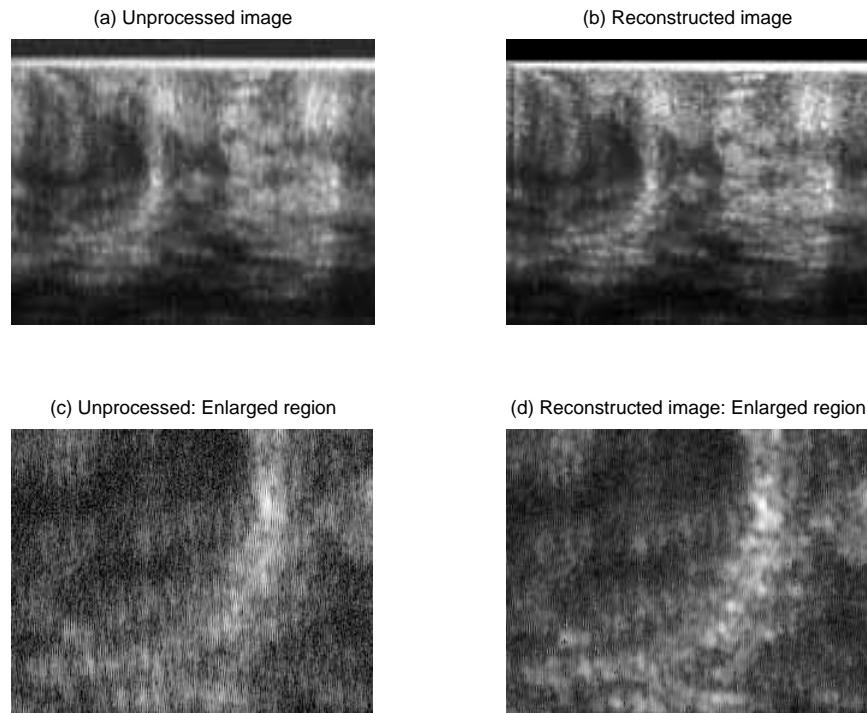


Figure 9. (a) Unprocessed OCT image of the skin of the finger, acquired *in vivo* with compression applied during every other A-line. (b) Image reconstructed by realigning displaced pixels, (c) and (d) Enlarged regions of upper images. The dimensions of the upper images are 1.2 mm (width)  $\times$  0.7 mm (depth). The intensities are mapped onto a logarithmic gray scale.

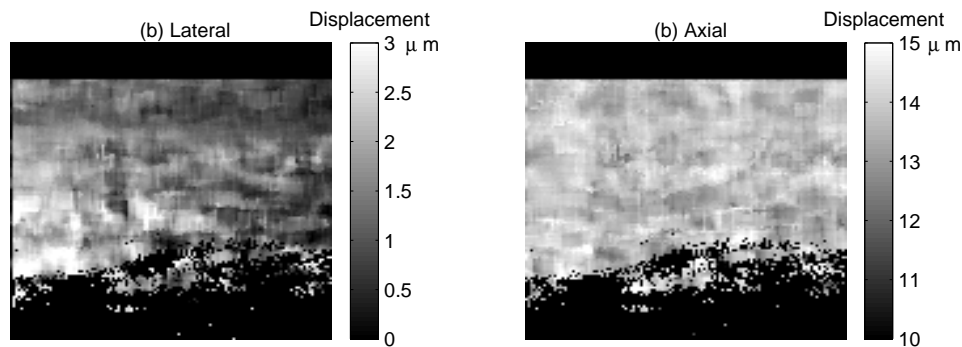


Figure 10. Images of (a) lateral and (b) axial displacement of the skin.

## 6. Summary and conclusions

This study explored the use of optical coherence tomography (OCT) for measurement of compressive deformation of tissue and tissue models on a micrometer scale. An experimental OCT elastography system was built that can image internal displacements as small as a few micrometers and differential strains of less than 1% inside of highly scattering media at depths up to about 1 mm. A hard mass embedded below the surface of a gelatin scattering model was shown to affect the deformation pattern observed in an image sequence acquired during gradual compression. This result suggests that a trained observer may be able to detect a subsurface cyst or hard nodule simply by viewing a sequence of OCT images captured while pressing on a tissue. To implement this technique *in vivo*, image acquisition speeds beyond the capability of our present system will be required. Detection of an imbedded object with an elasticity close to that of its surroundings is more challenging and requires quantitative analysis to determine the strain distribution. To estimate strain distributions in this study we applied speckle tracking methods similar to those developed previously for ultrasonic elastography. When data is collected in the line-by-line mode, these methods permit elastography of tissue to be performed *in vivo* even with slow-scanning OCT systems. Displacement images of skin derived from data collected in the line-by-line mode reveal a complex structure with features that reflect its layered structure. The signal-to-noise ratio of the measured strains was sufficient for quantitative measurement of differential strain within an area approximately 100  $\mu\text{m}$  deep and 50  $\mu\text{m}$  wide. Pushing the performance limits of the system to permit measurement of strain within smaller areas awaits improvements in the power and bandwidth of the light sources, faster scan speeds, and improved speckle tracking methods.

Possible medical applications of OCT elastography include differentiation of hard and soft masses during tissue biopsy, imaging of arterial plaque composition, and evaluation of scar tissue formation during wound healing. Additional studies are needed to evaluate the ability of OCT elastography to distinguish normal and pathological tissues *in vivo*. Except for those that pertain to the skin, most potential applications involve the use of an endoscope. To make OCT elastography compatible with these applications, new techniques need to be developed to apply a controlled mechanical stress to tissue at the distal end of an endoscope.